

Annual Review of Fluid Mechanics

Flows Over Rotating Disks and Cones

P. Henrik Alfredsson,¹ Kentaro Kato,²
and R.J. Lingwood¹

¹FLOW, Department of Engineering Mechanics, KTH Royal Institute of Technology, Stockholm, Sweden; email: phal@mech.kth.se, lingwood@mech.kth.se

²Department of Mechanical Systems Engineering, Shinshu University, Nagano, Japan; email: kentaro_kato@shinshu-u.ac.jp

ANNUAL
REVIEWS **CONNECT**

www.annualreviews.org

- Download figures
- Navigate cited references
- Keyword search
- Explore related articles
- Share via email or social media

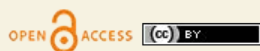
Annu. Rev. Fluid Mech. 2024. 56:45–68

First published as a Review in Advance on
September 15, 2023

The *Annual Review of Fluid Mechanics* is online at
fluid.annualreviews.org

<https://doi.org/10.1146/annurev-fluid-121021-043651>

Copyright © 2024 by the author(s). This work is licensed under a Creative Commons Attribution 4.0 International License, which permits unrestricted use, distribution, and reproduction in any medium, provided the original author and source are credited. See credit lines of images or other third-party material in this article for license information.



Keywords

boundary layer stability, cross-flow vortices, absolute instability, roughness, transition, turbulence

Abstract

Rotating-disk flows were first considered by von Kármán in a seminal paper in 1921, where boundary layers in general were discussed and, in two of the nine sections, results for the laminar and turbulent boundary layers over a rotating disk were presented. It was not until 1955 that flow visualization discovered the existence of stationary cross-flow vortices on the disk prior to the transition to turbulence. The rotating disk can be seen as a special case of rotating cones, and recent research has shown that broad cones behave similarly to disks, whereas sharp cones are susceptible to a different type of instability. Here, we provide a review of the major developments since von Kármán's work from 100 years ago, regarding instability, transition, and turbulence in the boundary layers, and we include some analysis not previously published.

1. INTRODUCTION

1.1. Background and von Kármán's Contribution

1/7-power law: a law relating the mean velocity increase normal to the wall as proportional to the wall distance raised to the power of 1/7

NS equations: the Navier–Stokes equations, including the continuity equation

Local wall velocity: $V_w^* = r^* \Omega^*$ in the laboratory frame of reference

The first scientific journal devoted to the field of solid and fluid mechanics was *Zeitschrift für angewandte Mathematik und Mechanik* (ZAMM). Its first volume was published in 1921 with six bimonthly issues. The driving force behind the journal was Richard von Mises, who at the time was a professor in applied mathematics at the University of Berlin [for a historical account of the start of ZAMM, see Siegmund-Schultze (2020)].

All articles in the first volume of ZAMM were written and published in the German language, and the list of authors reads like a who's who of German mechanics at the time. Many of the names are still well known today, such as Prandtl, Pohlhausen, Mohr, Trefftz, Mises, and von Kármán. Even though for the readers of this review most of these authors are known for their work in fluid mechanics, the work they published in ZAMM was spread across both solid and fluid mechanics.

Von Kármán's (1921) article *Über laminare und turbulente Reibung* [On laminar and turbulent friction; for an English translation, see von Kármán (1946)], was published in Issue 4 of Volume I as the first of six *Hauptaufsätze* (main articles). The original paper is close to 20 pages long and consists of 9 sections (note that there is a misprint in the paper, which has two sections numbered 8). Two of the sections deal with rotating disks, the first of which (section 7) develops the similarity theory for the solution of the laminar boundary layer on an infinite disk rotating in a still fluid, and the second (the first section 8 of the paper) discusses how the friction of a turbulent boundary layer on a rotating disk (hereafter, vKTBL) can be calculated using momentum conservation relations and the 1/7-power law for the velocity distribution. The other sections of the paper consider various aspects of wall-bounded flows, such as philosophical aspects of boundary layer theory, as well as boundary layers on flat surfaces and in pipe flows, smooth and rough surfaces, and heat transfer.

1.2. Setting the Scene

A rotating disk with angular velocity Ω^* (in the following, the superscript $*$ refers to a dimensional quantity) surrounded by a still fluid sets up a thin boundary layer flow close to the disk that is driven by the azimuthal wall shear stress at the disk surface. The boundary layer is 3D, and in addition to the main azimuthal velocity component, an outward radial flow is established due to the influence of the centrifugal force. The outward-moving fluid is replaced by an inflow normal to the disk surface from outside the boundary layer. One may see the disk as a simple (although inefficient) centrifugal pump.

Assuming laminar and steady flow, von Kármán showed that it is possible to reduce the Navier–Stokes (NS) equations to a system of ordinary differential equations by assuming that there is a self-similar solution independent of the radius by introducing a viscous length scale, $\delta^* = \sqrt{\nu^*/\Omega^*}$, where ν^* is the kinematic viscosity of the fluid. However, as the fluid moves radially outward the Reynolds number increases, and at some point an instability sets in, leading to transition and to turbulence. The transition on the disk occurs in an axisymmetric manner, i.e., the demarcation between the laminar and turbulent regions forms an almost perfect concentric circle around the rotational axis at some radius r^* , and there is a well-defined nondimensional radius ($R = r^*/\delta^*$ or, equivalently, a Reynolds number $Re_r = V_w^* r^*/\nu^* = R^2$, where V_w is the local wall velocity) for which it is not possible to keep the flow laminar. On the other hand, by introducing disturbances, such as surface roughness, the transition Reynolds number can be lowered.

From the perspective of practical applications the study of rotating-disk flows is mainly motivated by their similarity to the boundary layer flow on swept wings (see, e.g., Saric et al. 2003). In both cases there is an instability resulting in cross-flow vortices due to an inflection point in the

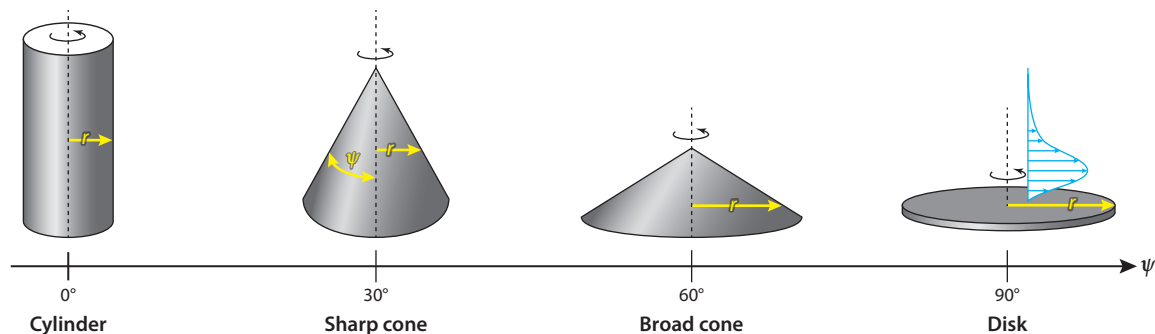


Figure 1

Various types of rotating geometrical bodies. Figure adapted from Kato et al. (2023).

mean velocity profile in the radial (cross-stream) direction. While von Kármán did not know the details of the transition to turbulence on the disk—it took until the mid-1950s until the cross-flow instability was discovered—such vortices seem to play a dominant role in the transition process both on swept wings and on rotating disks. In comparison with experiments on swept wings in wind tunnels, rotating-disk experiments provide a configuration with fewer variables, can be set up at a much smaller scale, and, therefore, can be housed in most fluid dynamics laboratories.

The flow over a rotating disk is a special case of a more general class of rotating bodies, spanning rotating cylinders, sharp and broad cones, and disks (**Figure 1**). Other geometrical shapes can also be encountered, such as the half-sphere, as well as convex or concave ogive cones (see, e.g., Kohama 2000).

However, there is also an even wider class of rotating flows of which the rotating disk is one part—namely, the so-called BEK family of rotating flows, named after Bödewadt (1940), Ekman (1905), and von Kármán (1921). The Bödewadt flow is that of a fluid in solid body rotation over a still, flat surface. Ekman (1905), on the other hand, was investigating the effect of Earth's rotation (Coriolis effect) on ocean currents, although in the present context Ekman flows are more related to the flow between two narrowly spaced rotating disks with slightly different rotational speeds. In the case with one rotating and one stationary disk with a large separation, usually called a rotor–stator system, a boundary layer of the Bödewadt type develops on the stationary disk and a von Kármán boundary layer develops on the rotating disk (see, for instance, Randriamampianina & Poncet 2006). Since the radial flow in the Bödewadt boundary layer is directed inward, toward the center of rotation, the Reynolds number decreases and the boundary layer relaminarizes near the center. For experimental work on the stability of the Bödewadt flow, the reader is referred to Savaş (1987) and Lingwood & Alfredsson (2000).

1.3. Limitations of the Review

There are only a few previous reviews of the boundary layer flow on various types of rotating bodies. Wimmer (1988) and Crespo del Arco et al. (2005) both provided general reviews of flows that are external, internal, and between rotating bodies of various geometrical shapes. Kobayashi (1994) dealt with the laminar–turbulent transition on rotating disks, cones, and spheres and mainly reported results from experimental studies. Lingwood & Alfredsson (2015) discussed instabilities in rotating-disk flow, with a special emphasis on the absolute instability discovered by Lingwood (1995). Recently Martinand et al. (2023) reviewed instabilities in rotating-disk boundary layers, with a focus on the connection to instabilities in cavities.

Absolute instability: an absolutely unstable disturbance is self-sustained and grows in time at a fixed spatial location, without being forced

Supplemental Material >

One limitation of the present review may be best described by a citation from Leonardo da Vinci (*Trattato della pittura*, section 29): “But it seems to me that those sciences are vain and full of errors which are not born of experience, the mother of all certainty, and which do not end in known experience.” Our perspective is to focus on rotating-disk and cone flows that are physically realizable and on the connection between experimental (and to some extent simulation) results and theoretical findings. We also review some theoretical and simulation results that are within the scope of realizable physical experiments but still need experimental verification. However, there are many theoretical/numerical studies that seem to lie beyond any achievable physical perspective, and those we leave outside the scope of this review. We also leave out early studies that deal with issues that are trivial today, such as calculations of the laminar boundary layer profile on a rotating disk. Finally, within the BEK family of rotating flows we limit ourselves to the “K,” although together with the disks we include both broad and sharp cones in a surrounding still fluid. The interested reader can find an expanded reference list in the **Supplemental References**.

2. BASICS

2.1. Definitions, Geometry, and Laminar Base Flow

The coordinates along and normal to the surface of a disk/cone/cylinder are shown in **Figure 2a**. The one parameter that defines the geometry is the half-apex angle ψ , which for the disk is $\psi = 90^\circ$ and for the cylinder is $\psi = 0^\circ$. As we see later in this review, there is demarcation between broad and sharp cones around $\psi = 45^\circ$ where the main instability changes from cross-flow dominated to centrifugally driven.

The length scale that was introduced by von Kármán (1921) to obtain the similarity solution for the laminar boundary layer on the disk is δ^* as defined in Section 1.2, and it normalizes both the radial, $r = r^*/\delta^*$, and wall-normal, $z = z^*/\delta^*$, distance. The azimuthal (V^*) and radial velocity (U^*) components are scaled with the local wall velocity (V_w^*), and in order to balance all terms in the continuity equation, the wall-normal velocity (W^*) needs to scale as $\sqrt{\nu^*\Omega^*}$, which also can be

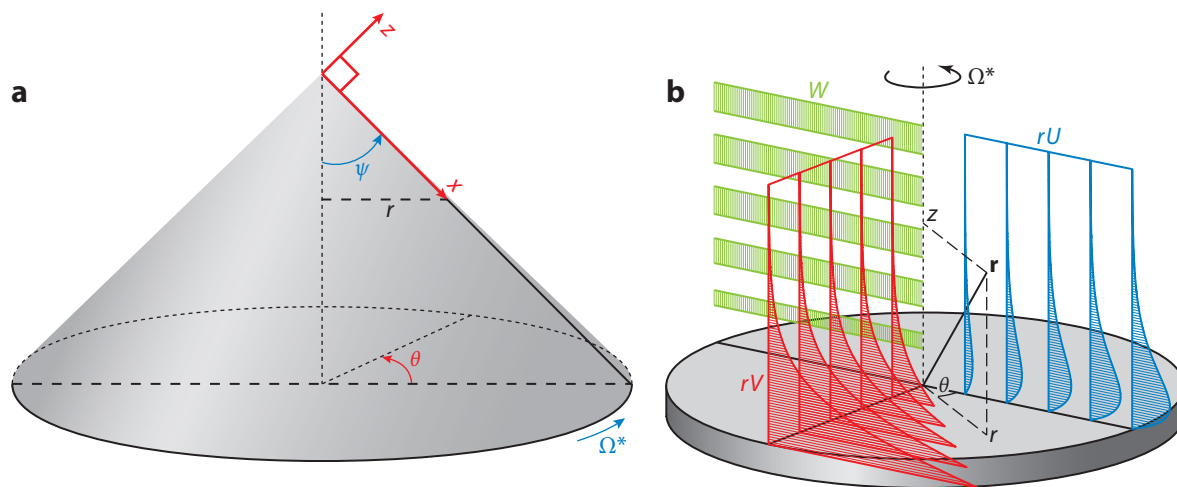


Figure 2

(a) Definition of various parameters for the cone flow; for the disk, we have $\psi = 90^\circ$ and $x = r$. (b) Sketch of laminar velocity field over a rotating disk in the laboratory frame. Note that the wall-normal velocity does not depend on the radius. Panel b adapted with permission from Imayama et al. (2014a).

written as $W = W^*/(V_w^* R)$. This shows that when R is large (i.e., away from the center of the disk), W is much smaller than V and U . Through these transformations and by noting that there are no variations in the azimuthal (θ) direction and that the pressure is constant in the radial (r) direction, we can transform the NS equations in the laboratory frame of reference into the following set of ordinary differential equations:

$$\begin{aligned} 2U + W' &= 0, & 1. \\ U^2 - V^2 + U'W - U'' &= 0, & 2. \\ 2UV + V'W - V'' &= 0, & 3. \\ P' + WW' - W'' &= 0, & 4. \end{aligned}$$

where $P = P^*/(\rho^* \nu^* \Omega^*)$ is the normalized pressure (ρ^* is the density of the fluid) and a prime (') denotes a z -derivative. The boundary conditions are $U = 0$, $V = 1$, and $W = 0$ on the disk ($z = 0$) and $U = V = 0$ as $z \rightarrow \infty$. A sketch of the velocity field is shown in **Figure 2b**. If the equations are expressed in the rotating system, the only difference is that V should be replaced by $V + 1$ in the equations and boundary conditions.

Wu (1959) realized that it is possible to generalize the viscous length scale such that a similarity solution can be formulated for the cone. If the length scale is defined as $\delta^* = \sqrt{\nu^*/(\Omega^* \sin \psi)}$ and the wall-normal velocity component is normalized as $W = W^*/\sqrt{\Omega^* \nu^* \sin \psi}$, Equations 1–3 that determine the velocity field become the same as those derived by von Kármán for the disk, although Segalini & Camarri (2019) proposed a self-similar correction valid in the tip region of the cone.

In Section 1.2, two different, but related, parameters to characterize the flow state on the disk were defined: a nondimensional radius and a Reynolds number. These can be generalized to the cone by normalizing the distance from the center of rotation r^* or apex of the cone (x^*) (note that $r^* = x^* \sin \psi$) with the viscous length scale $\delta^* = \sqrt{\nu^*/(\Omega^* \sin \psi)}$, giving a nondimensional distance, such that $R = x^*/\delta^* = \sqrt{x^* V_w^*/\nu^*} = x$. The other parameter is a Reynolds number Re_x , defined based on the length x^* and the local wall velocity V_w^* , giving $Re_x = x^* V_w^*/\nu^* = x^2$, i.e., $R = \sqrt{Re_x}$. Both have been used in the literature, although lately R is used more often.

In the above, a steady base flow is assumed; however, in an experiment the disk/cone must be started from zero velocity at a nondimensional time $t^* \Omega^* = 0$. Benton (1966) theoretically studied the transient of an impulsively started rotating disk and found that after about $t^* \Omega^* > 1.5$ the flow was fully developed. For quantitative experiments on the steady flow this does not present a problem, as there are no time limitations on how long the disk/cone can run before measurements are started. However, for flow visualizations, where some material is put on the surface before the disk/cone is rotating, this may have an influence. Nevertheless, by running such an experiment for a sufficiently long time, transient effects should be imperceptible.

2.2. Experimental Considerations

When planning a stability and transition experiment on a rotating cone/disk in a surrounding still fluid there are two competing criteria that need to be considered. First, the experiment should be able to achieve a Reynolds number high enough to reach well into the turbulent region so that the outer boundary of the rotating body does not unduly influence the stability and transition processes. Secondly, the thickness of the boundary layer has to be considered, especially if measurements inside the boundary layer are to be attempted practically. To exemplify this, let us for simplicity consider the rotating-disk case.

R_{edge} :
the nondimensional
radius at the edge of
the disk

For a clean disk—that is, a disk that has been polished so that the inherent roughness is of the order of one micron or less and where no artificial excitation of the boundary layer is applied—we know from previous experiments that the transition region ends around $R = 600$. Healey (2010) suggested that if R_{edge} is too close to the transition region it can affect the transition scenario. In an experimental study, Imayama et al. (2013) investigated three different geometrical edge configurations as well as various edge radii; however, no substantive effect on the transition Reynolds number due to the proximity of the edge was found. To be sure that the edge of the disk does not influence the instability and transition processes, however, one might still want to choose a setup with a fully developed turbulent region, such as $R_{\text{edge}} = 750$.

The laminar boundary layer thickness Δ^* is approximately equal to $3\delta^*$, which gives $R = 3x^*/\Delta^*$ or $\Delta^* = 3x^*/R$, showing that for a given nondimensional edge radius, R_{edge} , the laminar boundary layer thickness just depends on the radius at the edge, x_{edge}^* , and is independent of the fluid viscosity and the rotational rate of the disk. For a typical experimental setup the disk has a diameter of 0.5 m (i.e., $x_{\text{edge}}^* = 0.25$ m), which immediately gives us that the laminar boundary layer thickness is $\Delta^* \approx 1$ mm for $R_{\text{edge}} = 750$.

With a thin boundary layer, roughness on the surface may influence the flow quite substantially, so the quality of the surface needs to be controlled. It is also important that the disk/cone is well balanced; if not, a laboratory-fixed hot-wire sensor will move its relative distance from the surface during the rotation of the disk/cone.

3. FLOW VISUALIZATION AND TRANSITION ON ROTATING DISKS AND CONES

The first visualization of the flow on a rotating disk was made by Gregory et al. (1955) by applying a thin layer of a clay material that adhered loosely to the surface. The pattern from the clay revealed the flow near the surface and showed inclined structures (the number of structures was around 30), as well as a distinct radius where the clay was swept away by the higher wall friction where the boundary layer became turbulent (see **Figure 3a**). The motivation for their study was the analogy to a 3D flow in the swept-wing boundary layer, where the authors had also used the same flow-visualization technique and found that “narrow, regular traces are observed in the China clay picture” and concluded, “These traces appear to denote the presence of stationary vortices in the boundary layer” (Gregory et al. 1955, p. 161). **Figure 3b**, adapted from Imayama et al. (2014a), shows what was obtained from hot-wire measurements of the azimuthal velocity, measured on a clean disk at $z = 1.3$ and phase averaged over 1,000 revolutions. The color code indicates the deviation from the local mean velocity at each measured radial position. A pair of differently colored streaks corresponds to one cross-flow vortex, and these vortices are all corotating with varying development and strength. The vortex structures are stationary with respect to the disk despite the fact that there are no artificial roughnesses added to deliberately trigger them.

Gregory et al. (1955) found that the smallest R where the pictures showed traces of the instability is 421. The experiment was conducted at nine different rotational speeds spanning from 600 to 3,200 rpm and the average R for detection of the instability was 436 with a standard deviation of 15. Although the traces had somewhat different strengths and wavelengths, they concluded that the number of vortices was between 28 and 31. They also used a pressure tube connected to a microphone and from spectra found that the strongest signal corresponded to about 30 vortices. They compared these results with the hot-wire measurements by Smith (1947), who found a wave frequency with an average value of 32 from 13 different experiments, where both the radial position of the hot wire and the rotational speed of the disk were varied. He did not, however, at that point realize that the detected frequency was the result of stationary vortices passing by the

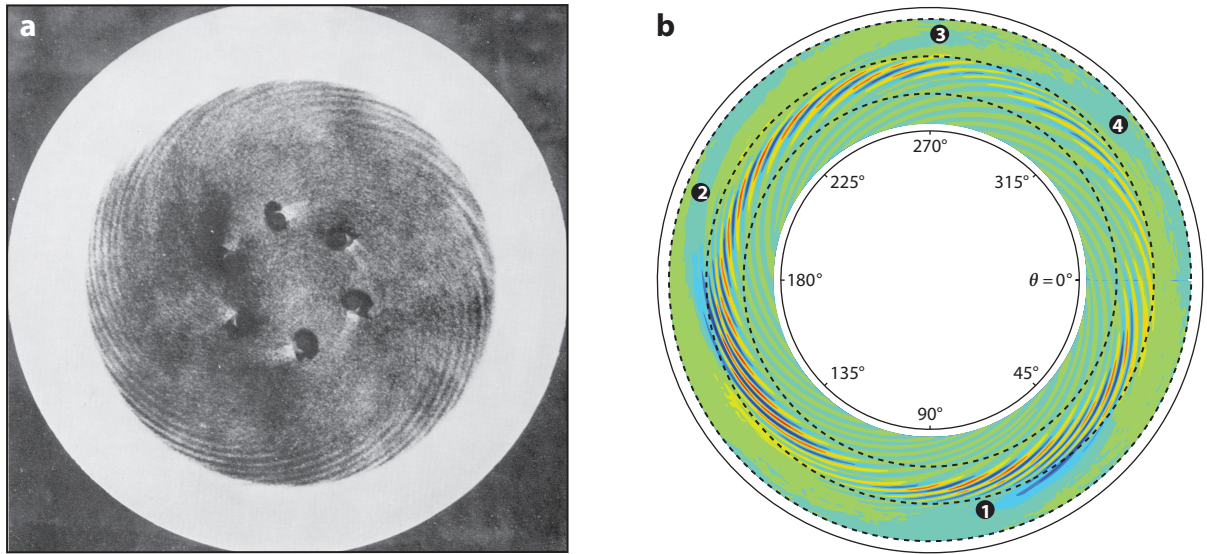


Figure 3

(a) Surface flow visualization for a disk rotating in still air where China clay is initially homogeneously deposited and dispersed through the action of the wall shear stress. The rotational direction is anticlockwise and the rotational speed is 3,200 rpm. The radius of the disk is 0.15 m, corresponding to a nondimensional radius of $R = x = 730$ at this rotational speed. Panel *a* adapted with permission from Gregory et al. (1955). (b) Cross-flow vortices on a clean disk obtained from hot-wire measurements of the azimuthal velocity at $z = 1.3$. The edge of disk is at $R = 731$. The color code indicates the deviation from the local mean velocity at each measured radial position. A pair of blue and yellow/red streaks corresponds to one cross-flow vortex. The numbers ①–④ in the outer turbulent region indicate weak large-scale structures that have also been observed in other experiments (see, e.g., Kobayashi et al. 1980, Corke & Knasiak 1998). Panel *b* adapted with permission from Imayama et al. (2014a).

laboratory-fixed hot wire. In their experiments, Gregory et al. (1955) found from the flow visualization patterns that the transition radius (the boundary separating the vortex region and the white region in **Figure 3a**) for the different cases is $R_{\text{trans}} = 533 \pm 8$.

In a series of papers from Japan, smoke flow visualizations and hot-wire measurements were carried out on disks and broad and sharp cones. Kobayashi et al. (1980) and Kobayashi & Izumi (1983) did experiments on a disk ($\psi = 90^\circ$) and several cones ($\psi = 15^\circ, 30^\circ, 45^\circ, 60^\circ$, and 75°) and determined the critical Reynolds number (i.e., at what radius vortices could be first detected) and transition Reynolds number (where the flow became turbulent), as well as the number of vortices. In **Figure 4**, photographs for a sharp cone ($\psi = 30^\circ$) (Kohama 2000) and broad cone ($\psi = 60^\circ$) (Kobayashi & Izumi 1983) are reproduced. As can be seen, both photographs show vortex-like structures; however, their appearances are quite different. For the sharp cone, the vortex structures seem to be wrapped around the cone, whereas for the broad cone the picture is similar to that of the disk. From flow visualization photographs, Kobayashi & Izumi (1983) also showed that vortices for a cone angle of 15° consisted of pairs of counter-rotating vortices, similar for example to Görtler or Taylor vortices, which indicates that vortices for sharp cones are the result of a centrifugal effect, rather than the 3D nature of the boundary layer.

In **Figure 5** critical and transition Reynolds number data for several studies are compiled and plotted versus cone angle. Here, we chose to use a slightly different definition of the Reynolds number ($Re_r = r^*{}^2 \Omega^* / \nu^*$) in order to be able to include data for the cylinder ($\psi = 0^\circ$) (Theodorsen & Regier 1944, Kirchner & Chen 1970). The data given in table 1 of Kobayashi & Izumi (1983) show that both the critical and transition Reynolds numbers decrease with decreasing

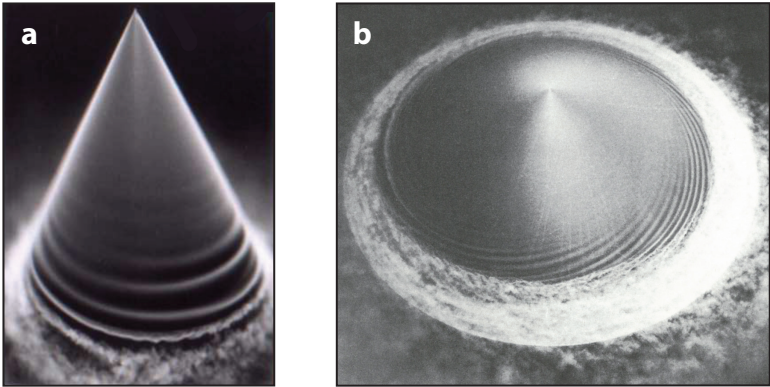


Figure 4

(a) Smoke flow visualization showing the instability and transition on a sharp cone (with a half-apex angle of $\psi = 30^\circ$). Rotation direction is anticlockwise (Y. Kohama, personal communication). Panel *a* adapted with permission by Current Science Association from Kohama (2000). (b) Smoke flow visualization showing the instability and transition on a broad ($\psi = 60^\circ$) cone. Rotation direction is anticlockwise. Panel *b* adapted with permission from Kobayashi & Izumi (1983).

Shape factor:
 $H_{12} = \delta_V / \vartheta_V$

cone angle, and below 45° this decrease is significant. We include the transition Reynolds numbers for the disk from Imayama et al. (2014a) and for the 60° and 30° cones from Kato et al. (2019b, 2021), respectively. For these experiments, the transition point is determined as the point where the boundary layer shape factor (i.e., the ratio between displacement thickness and

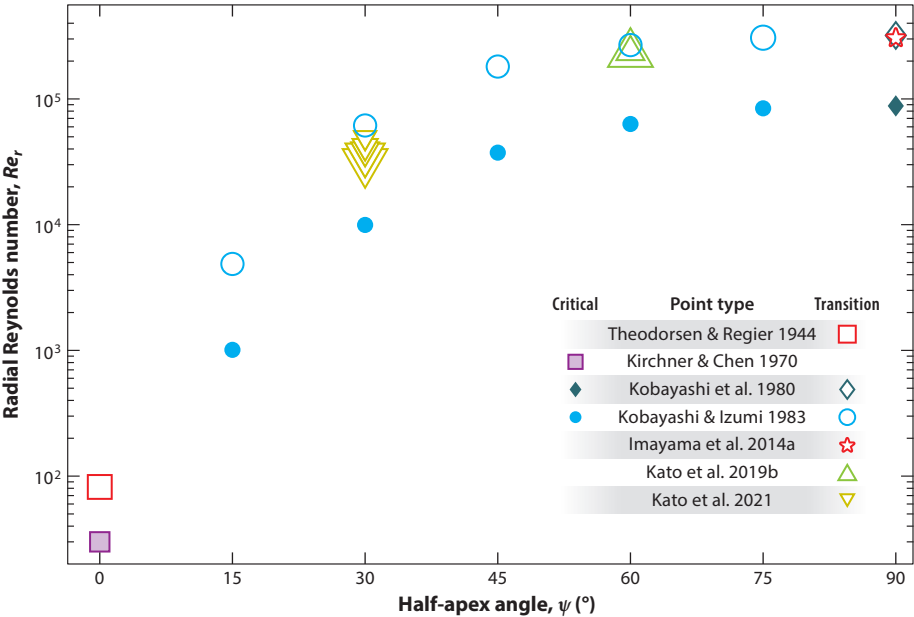


Figure 5

Measured critical points (filled symbols) and transition points (open symbols) on the cones with different half-apex angles ψ . The data of Kato et al. (2019b) are for angular velocity $\Omega^* = 900$ and 1,800 rpm; the data from Kato et al. (2021) are for $\Omega^* = 600, 750, 900, 1,500$, and 1,800 rpm.

momentum-loss thicknesses of the V profile) has deviated by 5% from its measured maximum value. The cone experiments were conducted with different rotational speeds and, as can be seen, the rotational speed did not influence the transition Re_r for the broad cone but has a strong influence (going from 600 rpm to 1,800 rpm) on the 30° cone, where it decreases with increasing rotation speed (the increasing size of the symbols indicates higher rotational speed).

For the disk, the critical radius for instability obtained by Kobayashi et al. (1980) is substantially lower ($R = 297$) than that observed ($R = 421$) by Gregory et al. (1955). This is probably due to hot-wire measurements being more sensitive and better able to detect smaller vortex amplitudes than the flow visualization technique used by Gregory et al. Notwithstanding, the transition radii observed by these researchers are of the same order (566 and 533, respectively) despite being obtained by different detection techniques. The slightly lower transition value observed by Gregory et al. (1955) might be explained by the fact that the China clay layer added roughness to the surface. The number of vortices reported by Kobayashi & Izumi (1983) was 31–32 for the disk, with the number decreasing with decreasing cone angle to 22–23 at 45°, and for the smaller cone angles ($\psi = 15^\circ, 30^\circ$) no cross-flow vortices were observed.

Displacement thickness:

$$\delta_V = \int_0^\infty V \, dz$$

Momentum-loss thickness:

$$\vartheta_V = \int_0^\infty (1 - V)V \, dz$$

4. STABILITY ANALYSIS AND TRANSITION SCENARIOS

Linear stability analysis is carried out by writing the perturbation quantities as

$$(u, v, w, p) = (\hat{u}, \hat{v}, \hat{w}, \hat{p}) \exp[i(\alpha x + \beta \theta - \omega t)],$$

where the eigenfunctions $(\hat{u}, \hat{v}, \hat{w}, \hat{p})$ are functions of z . In the following, the stability analysis is considered as a spatial problem where we have $\alpha = \alpha_r + i\alpha_i$, and α_r and α_i give the radial wavenumber and growth rate, respectively. The azimuthal wavenumber β corresponds to the number of vortices around the disk/cone and only takes integer values (positive, zero, or negative) due to the periodicity in the azimuthal direction. The perturbation frequency is $\omega = \omega^*/\Omega^*$, which is real for spatial analyses and complex for temporal analyses. When the analysis is carried out in the laboratory system of reference, disturbances that are stationary with respect to the disk fulfill the relation $\omega = \beta$. On the other hand, if the stability analysis is carried out in the rotating frame of reference, we have $\omega = 0$ for stationary disturbances.

4.1. Convective Instability on the Disk and Broad Cones

Neutral stability curves for stationary disturbances for the disk are shown in the α_r – R and β – R planes in **Figure 6a,b**. The neutral stability curves consist of two convectively unstable modes, usually denoted Type I and Type II, where the locus of Type I corresponds to the upper side, and partly to the lower side, of the neutral curve, and the locus of Type II takes over the lower side for R beyond the kink. The angle of the disturbance with respect to the azimuthal direction, $\epsilon = \tan^{-1}(\bar{\beta}/\alpha_r)$, with $\bar{\beta} = \beta/R$, is shown in **Figure 6c**. The Type I mode is an inviscid instability due to the inflection point in the radial velocity profile and gives rise to the cross-flow vortices that dominate in experiments. On the other hand, the Type II mode is a viscous mode and is caused by the streamwise curvature of the mean flow and Coriolis effects. Both types have unstable stationary and traveling disturbances relative to the disk surface, but the lowest critical Reynolds number for stationary disturbances is a Type I mode. For stationary disturbances only integer values of β are physically realizable; however, the stability equations can be solved for noninteger values. As can be seen from **Figure 6**, the most unstable stationary disturbance is of the cross-flow type, which first becomes unstable around $R = 285$ with $\beta = 22$. As R increases, higher wavenumbers also become amplified, which is consistent with experiments, where the number of vortices prior to transition is around 32 on the disk. The angle of the most unstable disturbance is around 12°. A

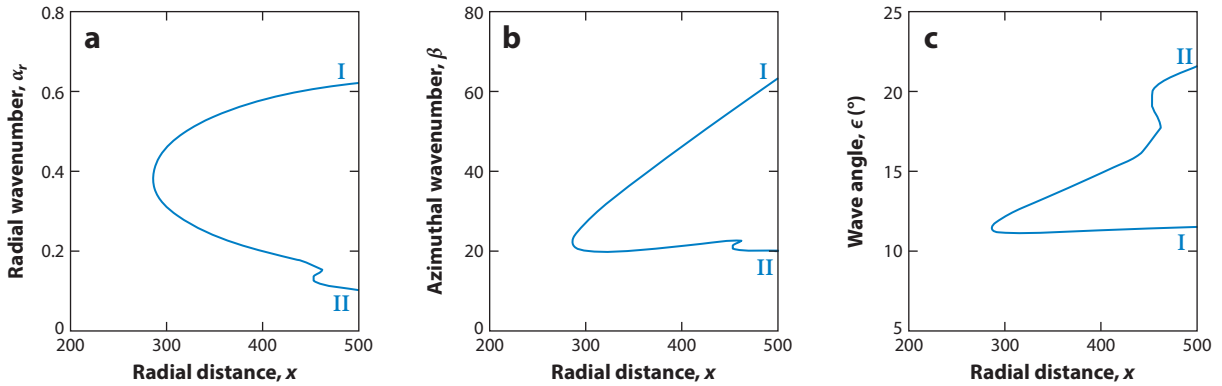


Figure 6

Neutral stability curves for the rotating disk of nondimensional wavenumbers α_r (a), β (b), and angle ϵ in degrees (c) versus x for stationary (in the rotating frame) disturbances. The loci for Type I and Type II modes are indicated along the curves. Figure adapted with permission from Appelquist et al. (2016b); copyright 2016 Elsevier Masson SAS. All rights reserved.

similar angle (14°) was observed by Smith (1947), who correlated the signals of two geometrically separated hot wires, and by Imayama et al. (2014a) (see their figure 13b), who determined the vortex angle of individual vortices (same data as in **Figure 3b**).

For broad cones the stability results are similar to the disk; although for $\psi = 60^\circ$ the critical R and β decrease to 265 and 19, respectively, according to Garrett et al. (2009).

4.2. Convective Instability on Sharp Cones

For sharp cones, Hussain et al. (2014) suggested that a different type of instability dominates below, say, $\psi \sim 40^\circ$ that is of centrifugal origin. This instability would give rise to pairs of counter-rotating vortices similar to Taylor or Görtler vortices, as visualized in the experiments undertaken by Kobayashi & Izumi (1983). Furthermore, Kato et al. (2021) made hot-wire measurements on a 30° cone and showed that instability and onset of transition are determined by a Görtler number.

This instability is different from the cross-flow modes, and Kato et al. (2021) found that the unstable mode that compared best with experiments was one with $\beta = -1$ (i.e., a traveling, almost ringlike mode with, in contrast to the cross-flow vortices, a small forward inclination corresponding to $\epsilon < 0$). Where $\beta = 0$ the disturbance is truly ringlike (i.e., with $\epsilon = 0$). Such a ringlike disturbance is observed in the flow visualization in **Figure 4a**.

4.3. Absolute Instability on the Disk

A search in the Web of ScienceTM using “rotating disk” as the publication title and “stability” as the keyword revealed that the two most cited papers (as of April 12, 2023) are those of Lingwood (1995, 1996) with 230 and 157 citations, respectively. The objective of those two papers was to investigate if the narrow-Reynolds number transition range observed in earlier experiments could be related to an absolute instability of the boundary layer flow. Lingwood (1995) developed the theory behind the absolute instability on the disk (via a spatiotemporal local stability analysis), which was then complemented with experiments in Lingwood (1996), where a pointwise impulsive disturbance was introduced through a small hole in the rotating disk that passed over an air jet below the disk. This excited a full range of frequencies repeatably and generated a wavepacket.

Lingwood (1995) found that there is a local linear absolute instability of the rotating-disk boundary layer at and beyond $R = 507$ for traveling modes with a dominating azimuthal

Görtler number:

$$G = \frac{V_{\theta}^* \partial_{r'}^*}{\nu^*} \sqrt{\frac{\partial_{r'}^*}{r^*}} = \sqrt{\frac{x \partial_{r'}^3}{\sin \psi}}$$

wavenumber with $\beta = 68$ at onset—the first absolute instability of any boundary layer flow to be found. The development of the wavepackets in the experiments also showed evidence of an absolute instability at about $R = 507$, indicating the onset of transition. These results can be viewed as a starting point for a large number of theoretical, experimental, and numerical studies up until the present day. Theoretically the absolute instability has subsequently been found in the rest of the BEK family (Lingwood 1997) as well as for rotating broad cones (Garrett & Peake 2007).

However, in experiments where traveling modes are not excited repeatably, the stationary cross-flow modes are dominant in visualizations and quantitative measurements in the convectively unstable region at Reynolds numbers below the onset of absolute instability. This makes the absolute instability hard to observe experimentally. Moreover, the absolute instability results from a linear stability analysis do not account for the spatial development of the boundary layer. This has spurred work to investigate the associated global and nonlinear behavior (for an introduction, see Huerre & Monkewitz 1990).

In the linear direct numerical simulation (DNS) by Appelquist et al. (2015), no stationary modes were excited but the flow was perturbed by an impulsive excitation and the simulation confirmed that the rotating-disk boundary layer can produce a linear amplified global mode with wavenumber $\beta = 68$; that is, the nonlocal spatial development of the flow is not sufficient to stabilize the evolution of the absolute instability found from the local stability analysis. Appelquist et al. (2016a) next included nonlinearity in the DNS of the rotating-disk boundary layer, again without excitation of the stationary cross-flow vortices. The results showed that the flow exhibited a nonlinear global instability at $R \sim 583$ (dependent on the nature of the outer turbulent region), i.e., above the onset of the local linear absolute instability at $R = 507$.

The experiments by Imayama et al. (2014a) showed growing traveling disturbances in the power spectra, which saturate around $R \sim 585$, whereupon turbulent breakdown of the boundary layer ensues. In the nonlocal and nonlinear DNS by Appelquist et al. (2018b), stationary cross-flow vortices were introduced through modeled roughness elements of various amplitude. There were differences for small- and large-amplitude roughnesses, but for all cases, the primary cross-flow instability was found to be convectively unstable, and secondary modes were found to be triggered spontaneously while the flow was developing; the authors proposed that this is a globally unstable secondary instability that leads to transition. This is in line with the analysis of Pier (2003), who suggested that transition coincided with the secondary absolute instability of the naturally selected primary nonlinear cross-flow vortices. In a later paper, Pier (2007) proposed that it might be possible to postpone transition by enhancing the amplitude of a primary instability of a different frequency and wavenumber from the naturally selected one, thereby potentially delaying the onset of the absolute secondary instability, as well as, therefore, transition.

4.4. Routes to Transition on the Disk and Broad Cones

In summary, these investigations on the rotating disk, which are likely to extend to the broad cone, suggest that there are two routes to transition. For the convective route, surface roughness excites the convectively unstable primary stationary cross-flow instability, leading to nonlinear saturation and then secondary absolute instability and transition to turbulence. The amplitude of the roughnesses determines the details, as shown by Appelquist et al. (2018b). For the absolute route, an absence of external forcing allows for a self-sustained primary absolute instability, a steep front, and a secondary absolute instability and transition. Both routes require an absolutely unstable region of sufficient radial extent; the former needs external forcing, and the latter is self-sustained [see Pier (2003, 2007), Appelquist et al. (2018b), and Martinand et al. (2023) for fuller details]. In practice, most experimental investigations have natural or artificially added roughness that promotes the convective route, hence the focus in Section 5.

DNS: direct numerical simulation, a simulation of the NS equations where all relevant scales (space and time) are resolved

Global instability: local stability analysis only applies to parallel and weakly nonparallel flows; global instability pertains to spatially developing flows

5. RECEPTIVITY, INSTABILITY AND TRANSITION

5.1. Illustrating Instability and Transition from Velocity Data

PDF: probability density function

The preferred way to obtain quantitative experimental data on instability growth and transition to turbulence is to measure the azimuthal velocity component ($V + v$) with a single stationary hot wire and use statistical or spectral methods to analyze the fluctuating part (v) of the signal. As shown by the flow visualizations in Section 3, the dominant features observed are stationary cross-flow vortices on both the disk and broad cones; however, that does not negate the fact that nonstationary instabilities exist. Once the measured signal is ensemble averaged (i.e., phase averaged over many revolutions of the disk/cone), the unsteady components are averaged out and a phase average of the steady flow field around the disk/cone is obtained; an example is shown in **Figure 3b**.

One way to illustrate the fluctuating signal from a stationary hot wire was introduced by Imayama et al. (2012), namely, a PDF (probability density function) plot where the PDF of v is followed in the downstream (radial) direction. This is illustrated in **Figure 7**, where two disk cases are shown, one with a clean surface and one where 32 small deterministic roughness elements are placed at $x = 287$ just upstream of the critical x for the convectively unstable stationary mode. The data are taken at $z = 1.2$, which is close to the z -position of the maximum disturbance amplitude. In both cases, the PDF initially widens symmetrically (close to exponential) as the disturbances grow with increasing x until there is a clear asymmetrical change at a distinct x , where the PDF becomes highly skewed. In this region the PDF also has its maximum width. As x increases further the PDF becomes rather symmetric again, which is an indication that the flow has become fully turbulent. The overall appearance for the two cases is similar although the PDF picture is shifted to lower x for the case with roughnesses. An interesting observation is that at the end of the exponential growth the roughness case shows two maxima, one on each side of the center, whereas for the clean case there is only one maximum at the center of the PDF. This can

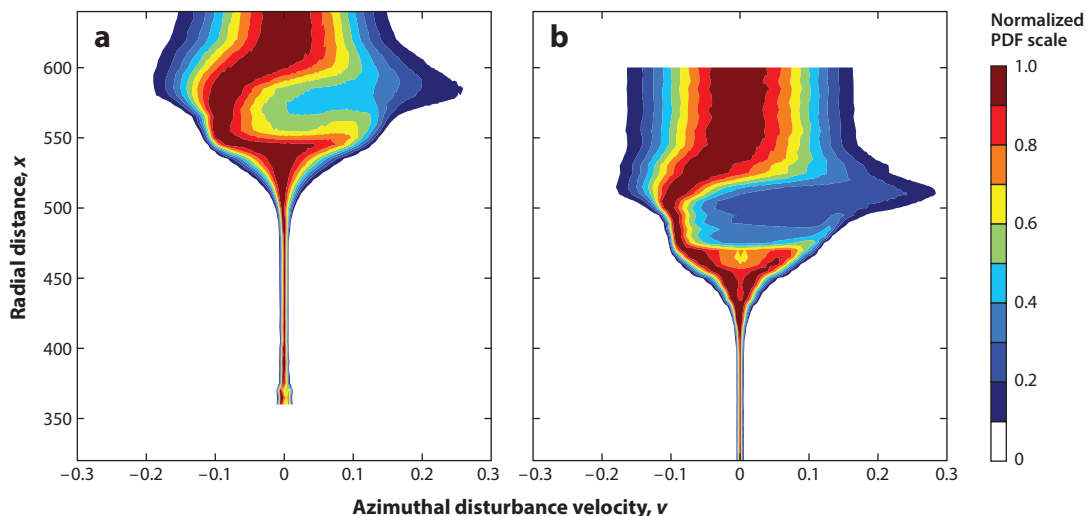


Figure 7

A PDF (probability density function) plot of the azimuthal disturbance velocity for the rotating disk as a function of downstream distance for (a) clean case and (b) a case with regularly spaced deterministic roughness. For each x the PDF is normalized with its maximum value. Panel a adapted with permission from Imayama et al. (2012). Panel b data are from Imayama et al. (2016). Both panels are based on unfiltered data.

be explained by the fact that the roughnesses lock the cross-flow vortices in space and they all have similar strengths, giving a disturbance velocity signal that is close to sinusoidal; a PDF of a sinusoidal signal has two maxima, one for $-\pi/2$ and another for $+\pi/2$. For the clean case, on the other hand, the vortices may originate from different radii and may therefore have different amplitudes (as seen in **Figure 3b**) and be less steady in the azimuthal direction, therefore giving rise to a PDF with a more Gaussian-like distribution (Kato et al. 2019b). The PDF plot can be used to define where transition starts and ends, and for the cases in **Figure 7a,b**, the start of transition can be estimated as $x = 550$ and 470 , respectively. The end of transition is not as sharp but can be estimated as $x = 625$ and 550 for the two cases. The PDF plot can also be used for cones: Broad cones produce plots similar to those for the disk but are shifted toward lower x , and sharp cones produce a somewhat less distinct behavior, especially for the end of transition (Kato et al. 2023).

A more detailed view of the flow development can be obtained from space–frequency spectral plots, where it is possible to see which wavenumbers are the most unstable; note that for stationary disturbances, in the laboratory frame we have $\beta = \omega$. In the left column of **Figure 8** space–frequency spectra for three cases (all with clean surfaces) are shown: the disk, the broad cone, and the sharp cone. For the disk and the broad cone, the most unstable disturbances show up as a

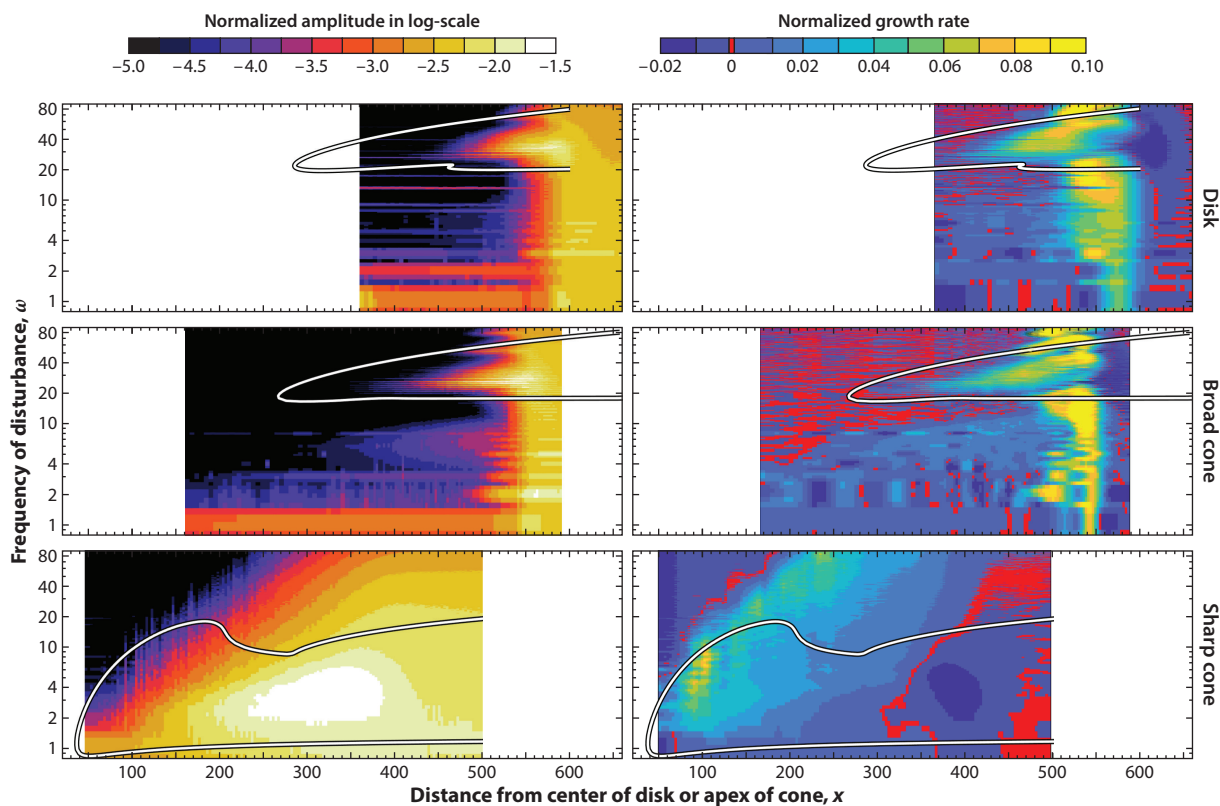


Figure 8

Space–frequency diagram of amplitude spectra (normalized with the local wall velocity V_w at each x) in logarithmic-scale (left column) and the growth rate (right column) for the azimuthal disturbance velocity for the disk (top), broad 60° cone (middle), and sharp 30° cone (bottom). Rotational speed is 1,400 rpm for the disk and 900 rpm for both cones. All cases are for a clean surface. Also shown is the neutral stability curve for stationary disturbances on the disk and the broad cone and for $\beta = -1$ for the sharp cone. Data from Kato et al. (2023).

Roughness Reynolds number:

$Re_{kk} = k^* \mathcal{V}_k^* / \nu^*$, with k^* the roughness height and $\mathcal{V}_k^* = V_w^* - \sqrt{(V_k^{*2} + U_k^{*2})}$ the undisturbed mean velocity at $z^* = k^*$

ridge around $\omega = 32$ and $\omega = 26$, respectively. Additionally, higher harmonics of these frequencies appear as x increases. The most dramatic feature is how the spectra fill up for all frequencies at a specific x for both cases, which is a sign that the beginning of transition is quite distinct—compare the spectrum for the disk in the top left of **Figure 8** and the PDF plot in **Figure 7a**, both of which show a distinct transition around $x = 550$. The spectrum for the 30° cone, however, has a qualitatively different behavior; it shows no distinct frequencies but develops gradually toward higher frequencies as x increases. There is a maximum in the spectrum around $\omega = 4$ at $x \sim 330$. The right column of **Figure 8** shows the growth rate calculated from the spectra. In all figures a neutral stability curve has also been included—for the disk and broad cone it is shown for the stationary modes, whereas for the sharp cone the curve is for $\beta = -1$ (see Section 4.2).

5.2. Discrete Roughness Elements

Naturally occurring random roughnesses on the surface of a rotating disk, even on a well-polished clean disk, have been found to give rise to stationary cross-flow vortices. In order to have a deterministic wave pattern, several experiments have employed regularly spaced (in the azimuthal direction) small roughness elements attached to the disk/cone surface, typically at a smaller radius than the critical radius for growth of stationary disturbances of that particular wavenumber. The number of roughness elements then gives the wavenumber (β) of the vortices, which is typically chosen to be close to the wavenumber that is observed naturally developing on the clean surface. For a typical experiment in air, the roughness height (k^*) can be of the order of $10 \mu\text{m}$, triggering stationary and uniform cross-flow vortices despite being of the order of only 3% of δ^* (or, equivalently, 1% of the laminar boundary layer thickness). In some experiments larger roughness heights have been used; for instance, Corke & Knasiak (1998) used $k = k^*/\delta^* = 0.16$. In that experiment two different wavenumbers were chosen, $\beta = 19$ and 27 ; the former was chosen because that wavenumber is close to the minimum critical Reynolds number for cross-flow growth. If one triggers with such a small β one can expect β to increase as x increases, which is also observed for natural disturbances (see, e.g., Malik et al. 1981).

Another scenario is obtained by introducing a single roughness element. Jarre et al. (1996) introduced one rather large cylindrical element with $k = 1.28$ at $x = 250$, showing a strong localized wave in the hot-wire signal just downstream of the roughness element, after which a wavepacket formed that increased in width azimuthally as it traveled radially outward. In contrast, Imayama et al. (2016) used a small single roughness element with a height of $k = 0.014$. A similar wavepacket spread outward in this case but with an initially much smaller amplitude, and breakdown to turbulence occurred at a higher R than in the experiments conducted by Jarre et al. (1996).

In the experiments by Kato et al. (2022) on a 60° cone, 24 roughness elements were equally spaced in the azimuthal direction at $x = 267$, whereas the critical x for this wavenumber is 286. In those experiments three roughness heights were used with approximately $k_1^* = 4$, $k_2^* = 8$, and $k_3^* = 16 \mu\text{m}$, corresponding to roughness Reynolds numbers $Re_{kk} = 0.018$, 0.072 , and 0.28 , respectively. In a laminar 2D boundary layer a disturbance resulting from such a small roughness Reynolds number would soon diffuse without giving any residual disturbance. The answer to why the disk/broad cone boundary layer is much more receptive to small localized roughness elements seems to be linked to the three-dimensionality of the mean flow. Here, it is noteworthy that the 3D boundary layer on swept wings is also susceptible to minute roughnesses, which are sufficient to generate cross-flow vortices (see for instance Saric et al. 2003).

The amplitude of the fundamental ($\omega = 24$) and the first harmonic ($\omega = 48$) for the three roughness heights mentioned above is shown in **Figure 9a** together with the results for the clean

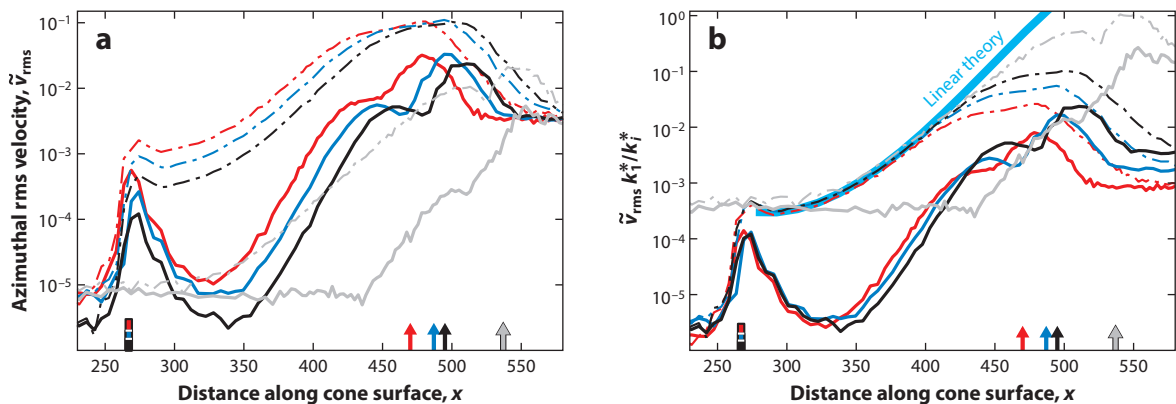


Figure 9

(a) The amplitude of the fundamental (*dash-dotted line*) and first harmonic (*solid line*) for four cases obtained from phase-averaged data (\tilde{v}) of the fluctuating azimuthal velocity: the clean cone (*gray*) and three cases with 24 deterministic roughness elements spaced equally in the azimuthal direction at $x = 267$, shown as a rectangular box on the abscissa. The three cases have one (*black*), two (*blue*), and four (*red*) layers of Letraset dots, giving a sequence of approximately 1:2:4 in respective roughness heights k_1 , k_2 , and k_3 . (b) The amplitudes normalized with the height of the roughness elements. The equivalent height for the clean case was estimated by fitting the curve to the others in the linear region. The wide blue line shows how the amplitude develops according to linear theory. The figure is based on data from Kato et al. (2019a) and Kato et al. (2023). The colored arrows on the abscissa show the estimated transition points for the different cases based on spectral data.

cone for the same frequencies. The figure shows that there is a strong increase in amplitude around the roughness element at $x = 267$ for both frequencies, although the harmonic soon reduces back to a level similar to that upstream of the elements. After a slight dip downstream of the roughness, the amplitude of the fundamental starts to grow exponentially.

The same data are shown in **Figure 9b** but the amplitude has been normalized with the height of the roughness elements, i.e., k_1/k_i ($i = 1, 2, 3$), where the smallest $k_1^* = 4 \mu\text{m}$ is used as the normalizing height. This normalization makes the fundamental for each of the three roughness cases overlap in the linear region, showing that the receptivity is linear for these roughness heights. **Figure 9b** also shows how the amplitude develops according to linear theory and that there is a good agreement between theory and experiment. The linear region allows the effective roughness height on the clean cone (k_0) to be estimated by fitting the curve for the fundamental frequency to overlap with those for the roughness elements. In this manner the equivalent roughness height for the clean cone was determined as $k_0 = 0.08 \mu\text{m}$. As expected, the first harmonics for the different roughness heights (not shown) in the linear region scale if the amplitude is normalized with $(k_1/k_i)^2$. Kato et al. (2022) also estimated the transition point based on spectral data and this position is shown in **Figure 9**. The **Supplemental Video** to this article shows the development of the disturbance velocity on the cone with 24 roughness elements as x increases.

Supplemental Material >

5.3. Distributed Roughness and Compliant Walls

Watanabe (1989) experimentally studied disks rotating in still ambient air with distributed roughnesses with different heights in the range of $1.8\text{--}15 \mu\text{m}$. The value of δ^* , by comparison, was about $200 \mu\text{m}$, meaning that the roughness height is a small fraction of δ^* . Both the critical (where the first oscillations were observed in the hot-wire signal) and the transition (where the hot-wire signal became fully chaotic) Reynolds numbers were determined and found to decrease with increasing roughness height. The number of vortices in the transition region was also determined

and showed a decrease with increasing roughness height, from 32 for the clean case to 25 for a roughness height of 15 μm . This might be a result of the distributed roughness exciting a range of unstable wavenumbers with the potential for a smaller wavenumber being amplified at lower radius and dominating through the transition process (cf. **Figure 6b**).

This study was followed by experiments on cones ($\psi = 60^\circ$ and 45°) with roughness heights in the range of 4–19 μm (Watanabe et al. 1993). The results for smooth surfaces were also included, and in all cases it was found that, as for the disk, both the critical and transition Reynolds numbers decreased with increasing roughness height and that there was a similar decrease in the number of vortices.

The effect of distributed roughness on the velocity flow field has been studied theoretically by changing the boundary condition at the wall. Miklavčič & Wang (2004) suggested a partial-slip condition instead of the no-slip condition at the disk surface, which can be applied in both the radial and azimuthal directions and thereby simulate both isotropic and anisotropic roughness distributions. In practice, this approach corresponds to a change of the mean velocity profiles. Yoon et al. (2007) adopted another approach and solved the boundary layer equations for the particular case of an axisymmetric, sinusoidal-shaped wavy surface. A more general approach was suggested by Chicchiero et al. (2021), who investigated the influence on the mean velocity field around a single roughness element using triple-deck theory and verified the results with DNS. They suggested that with this method a random distribution of roughnesses could be simulated.

Linear stability analyses using the approach by Miklavčič & Wang (2004) were undertaken by Cooper et al. (2015) for the disk and by Al-Malki et al. (2022) for broad cones. They found that in both cases the Type I mode (cross-flow mode) is stabilized, whereas the Type II viscous mode seems to become destabilized by concentric grooves (slip in the azimuthal direction). Harris et al. (2012) combined theory and experiments in the spirit of Yoon et al. (2007). In their water experiments three aluminum disks with concentric sinusoidal grooves of different depths (in the approximate range of 0.1–0.48 λ) were used. Spectra from hot-film measurements showed that the dominant frequency (corresponding to cross-flow vortices passing by the stationary hot film) was lower for the rough disk (~ 26) than for the smooth disk (~ 30) and that, for the rough disk, the disturbances were detectable for smaller R . However, none of these studies using linear stability analysis have so far been able to shed much light on the instability observed in experimental studies, where small and localized roughnesses are the primary sources of the cross-flow vortices leading to transition.

Another way to change the boundary conditions is to replace the rigid wall with a compliant wall. The interest in this stems from the possibility to delay transition or reduce turbulent drag after transition. Experimental, theoretical, and numerical work for the disk has been conducted, and an extensive review of such work has been given by Carpenter & Thomas (2007). The interested reader is referred to that publication, but here it is worth saying that stability theory shows that the Type I modes are stabilized by compliance, whereas the effects on Type II modes are more complex; depending on the magnitude of compliance, Type II modes can be destabilized (for low levels of compliance) or stabilized (for high values). Furthermore, experimental studies are inconclusive; some experiments could be interpreted as showing that compliance delays transition, and others that transition occurs at an R that is lower for a compliant surface than for a rigid one. Experiments are, of course, quite complex since the material properties of the compliant wall are of utmost importance for the results.

6. TURBULENT BOUNDARY LAYERS ON THE ROTATING DISK

The early works on vKTBL on the rotating disk dealt mainly with the frictional resistance using torque measurements (see, e.g., Theodorsen & Regier 1944). Experimentally, it is relatively

uncomplicated to measure the total resistance of a rotating disk by measuring the torque needed to rotate it with a given rotational speed. One should, however, remember that when measuring the torque one gets the collective contributions from the laminar, transition, and turbulent regions (of both sides) on the disk, as well as the rim. The main contribution, however, comes from the outer (turbulent) part of the disk since both the wetted area and the speed increase with r^* , meaning that the contribution to the torque from a band with width Δr^* is approximately proportional to $r^{*4} \Delta r^*$.

When it comes to detailed studies of the vKTBL there is a handful of experimental studies reported in the literature (Cham & Head 1969, Erian & Tong 1971, Itoh & Hasegawa 1994, Littell & Eaton 1994, Chiang & Eaton 1996, Imayama et al. 2014b) that have reported mean velocity and turbulence distributions. Additionally there exists one DNS study (Appelquist et al. 2018a) of the vKTBL.

6.1. Integral Relations

Von Kármán (1921) derived two integral relations: One is based on the balance between the change of radial flux of angular momentum leaving and entering an annular volume between $r^* + dr^*$ and r^* and the torque exerted by the mean azimuthal wall shear stress ($\tau_{w,\theta}^*$) acting on the disk surface of that volume:

$$2\pi\rho^*\frac{d}{dr^*}\left(r^{*2}\int_0^\infty U^*V^*dz^*\right) = -2\pi r^{*2}\tau_{w,\theta}^*. \quad 5.$$

The second is where the change in the radial momentum flux and the centrifugal force balance the radial mean wall shear stress ($\tau_{w,r}^*$):

$$\rho^*\frac{d}{dr^*}\left(r^*\int_0^\infty U^{*2}dz^*\right) - \rho^*\int_0^\infty V^{*2}dz^* = -r^*\tau_{w,r}^*. \quad 6.$$

Equations 5 and 6 can be rewritten in terms of nondimensional quantities as

$$\frac{d\Theta_{UV}}{dr} + \frac{4\Theta_{UV}}{r} = \tau_{w,\theta} = -\frac{1}{r}\frac{\partial V}{\partial z}\Big|_{z=0}, \quad 7.$$

$$\frac{d\Theta_{UU}}{dr} + \frac{1}{r}(3\Theta_{UU} - \Theta_{VV}) = -\tau_{w,r} = -\frac{1}{r}\frac{\partial U}{\partial z}\Big|_{z=0}. \quad 8.$$

Here, $\tau_{w,\theta}$ and $\tau_{w,r}$ are the (mean) nondimensional wall shear stresses normalized by $\rho^*V_w^{*2}$. The integral quantities are given as

$$\Theta_{UV} = \int_0^\infty UV dz, \quad 9a.$$

$$\Theta_{UU} = \int_0^\infty U^2 dz, \quad 9b.$$

$$\Theta_{VV} = \int_0^\infty V^2 dz. \quad 9c.$$

The same integral relations were derived by Cham & Head (1969) directly from the NS equations in the rotating frame of reference. In **Table 1**, the values of the three integral quantities in Equations 9a–9c are given both for the von Kármán similarity boundary layer (vKSBL) and for two cases ($x = 464$ and 669) of the vKTBL based on the DNS by Appelquist et al. (2018a).

Table 1 Integral quantities for the vKSBL and vKTBL^a

Boundary layer	$\Theta_{UV} = \int_0^\infty UV \, dz$	$\Theta_{UU} = \int_0^\infty U^2 \, dz$	$\Theta_{VV} = \int_0^\infty V^2 \, dz$	$\partial V / \partial z _{z=0}$	$\partial U / \partial z _{z=0}$
vKSBL	0.154	0.0541	0.672	-0.616	0.510
vKTBL, $x = 464$	0.229	0.0956	0.78	-1.09	0.42
vKTBL, $x = 669$	0.271	0.107	0.90	-1.36	0.41

^avKTBL values are based on the DNS by Appelquist et al. (2018a). Here, U and V are the radial and azimuthal velocities, respectively. Abbreviations: DNS, direct numerical simulation; vKSBL, von Kármán similarity boundary layer; vKTBL, von Kármán turbulent boundary layer.

For the vKSBL, both $d\Theta_{UV}/dr$ and $d\Theta_{UU}/dr$ are equal to zero and the data in **Table 1** show that Equations 7 and 8 are fulfilled by the von Kármán similarity solution. For the vKTBL, on the other hand, the derivatives are not zero, but positive. In order to fulfill Equation 7, the derivative term needs to contribute about 15–20% to the left-hand side (LHS), and even more to the LHS of Equation 8. These results indicate an initial rapid growth of the turbulent boundary layer.

6.2. General Considerations for Experiments

The Reynolds number on a rotating disk $Re_x = V_w^* x^* / \nu^*$ varies as x^{*2} , and even a small apparatus can reach high values. For instance, a disk with a diameter of 1,000 mm rotating with 1,000 rpm in air would have an $Re_x = 1.7 \cdot 10^6$ at the edge. However, one should be aware that this Reynolds number is not equivalent to a Reynolds number based on the distance from a leading edge and free-stream velocity of a 2D turbulent boundary layer (2DTBL); a detailed comparison, for instance, of the statistics between these two cases would be best undertaken by a comparison for similar Reynolds numbers based on a boundary layer parameter (e.g., the momentum-loss thickness for a 2DTBL and ϑ_V^* for the vKTBL).

For experimental studies of the velocity distributions and other statistical quantities an important parameter is the inner length scale, $\ell^* = \nu^* / v_\tau^*$, where $v_\tau^* = \sqrt{\tau_{w,\theta}^* / \rho^*}$ is the friction velocity in the azimuthal direction. This can also be written using the friction coefficient $c_{f,\theta} = 2(\nu_\tau^* / \Omega^* x^*)^2$ as

$$\ell^* = \sqrt{\frac{2}{c_{f,\theta}}} \frac{\nu^*}{\Omega^* x^*} = \sqrt{\frac{2}{c_{f,\theta}}} \frac{x^*}{Re_x}, \tag{10}$$

where $c_{f,\theta}$ is expected to be a weak decreasing function of the Reynolds number for a smooth disk. Hence, for a given Ω^* the viscous length scale varies approximately as $1/x^*$. This is a much stronger variation than for a 2DTBL and it varies in the opposite direction; with increasing Reynolds number the inner scale becomes smaller, which is in contrast to a 2DTBL developing along a flat plate.

For measurements at a specific value of Re_x , Equation 10 shows that measurement at a large x^* also gives a larger inner length scale. For turbulence measurements it is then obvious that an experimental setup should be designed to have a large diameter disk to get a large inner scale, but also to be able to do the measurements sufficiently far away from the transition region, but not too close to the edge.

The variation of ℓ^* with x^* has implications for torque-measuring techniques for determination of the friction of rough surfaces. Since the inner length scale decreases with radius, the nondimensional roughness height ($k^+ = k^* / \ell^*$) increases. This fact makes the results of such torque measurements challenging to evaluate.

2DTBL:
two-dimensional
turbulent boundary
layer

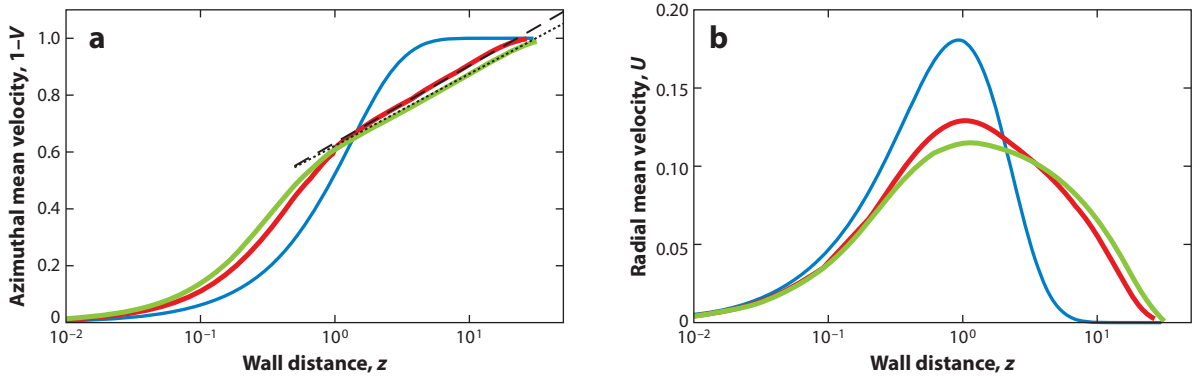


Figure 10

Distributions of (a) the azimuthal ($1 - V$) and (b) radial (U) mean velocity components on a rotating disk as a function of wall distance z . Two Reynolds numbers for vKTBL are shown, $x = 464$ (red line) and $x = 669$ (green line), based on the direct numerical simulation by Appelquist et al. (2018a). The logarithmic velocity is also plotted using $1 - V = v_\tau [\frac{1}{\kappa} (\ln zrv_\tau) + B]$, with $\kappa = 0.41$ and $B = 5.5$, as dashed and dotted lines in panel *a*. The von Kármán similarity solution for the laminar boundary layer is shown as a blue line. Note that the maxima of U seem to be located at $z \approx 1$ for all cases.

6.3. Experimental and Numerical Results

Overall one can say that the azimuthal mean velocity component and its higher moments show close similarity to the zero-pressure gradient 2DTBL, as shown by Appelquist et al. (2018a), who compared DNS, rotating-disk experiments by Imayama et al. (2014b), and those on the 2DTBL by Schlatter & Örlü (2010) via plots in wall variables—i.e., scaled as $(V_w^+ - V^+) = (V_w^* - V^*)/v_\tau^*$ and $z^+ = z^*v_\tau^*/\nu^*$, and similarly for higher moments. The plots show good agreement between the DNS and experiments including the 2DTBL in the near-wall region as well as in the logarithmic region. However, in the outer part of the boundary layer the wake component for the rotating-disk profiles is nonexistent. This has been observed for all studies that have shown the mean azimuthal velocity distribution in the linear-log format. The lack of a wake region seems to be a distinct feature of the vKTBL.

Figure 10a,b shows the mean of both the azimuthal and radial velocity components for the vKTBL at two Reynolds numbers [$x = 464$ and 669 , based on Appelquist et al. (2018a)] as well as for the vKSBL. Here, the velocity data are scaled with V_w^* and the wall distance is scaled as $z = z^*/\delta^*$. In the viscous sublayer, the velocity profiles for both the radial and azimuthal velocity are linear and can, in the above scaling, be written respectively as

$$U = zru_\tau^2 \quad \text{and} \quad 1 - V = zrv_\tau^2.$$

The data of Appelquist et al. (2018a) show that the azimuthal velocity adheres to the linear profile in the viscous sublayer up to $z_\theta^+ \sim 5$, whereas the U profile deviates from the linear profile closer to the wall.

In **Figure 10a** the logarithmic line is also plotted but here transformed into the present coordinates as

$$1 - V = v_\tau \left[\frac{1}{\kappa} (\ln zrv_\tau) + B \right],$$

with $\kappa = 0.41$ and $B = 5.5$. As mentioned above, the wake region is nonexistent for the vKTBL. An interesting result shown in **Figure 10b** is that the radial velocity component has its maximum close to $z = 1$ both for the vKSBL and vKTBL; that is, the maximum's physical distance from the surface of the disk is nearly constant independent of whether the boundary layer is laminar or

Scaling: length scale relationships:
 $z_\theta^+ = zrv_\tau$, $z_r^+ = zru_\tau$

turbulent [see also figure 5*a* of Appelquist et al. (2018a)]. This is despite the fact that the thickness of the vKTBL is an order of magnitude larger than the laminar boundary layer.

7. SUMMARY AND FUTURE DEVELOPMENTS

Although it is now more than one hundred years since von Kármán published the similarity solution of the laminar boundary layer on a rotating disk, the flow around rotating disks and cones is still a vibrant, and also expanding, field of research. Many aspects of the flows are still unanswered or less investigated, and we foresee that research on many aspects of rotating bodies will be an active area for a long time, where experiments, simulations, and theory will play important roles.

SUMMARY POINTS

1. The instabilities on disks and broad cones are similar—both dominated by a cross-flow instability in experiments. The boundary layers for these cases are highly receptive to surface roughness, which has a strong influence on the transition location.
2. Sharp cones are susceptible to a centrifugal instability governed by a Görtler number. The azimuthal wavenumber of that instability is found to be much smaller than that of the cross-flow instability, and transition occurs at smaller Reynolds numbers.
3. Despite its three-dimensionality, the mean and higher statistics of the azimuthal velocity of the turbulent boundary layer are similar to that of the 2D flat plate boundary layer except in the outer, wake, region. The three-dimensionality does not seem to play an important dynamic role.

FUTURE ISSUES

1. The breakdown to turbulence of the cross-flow vortices for the disk and broad cones and the importance of the local linear absolute instability in this global nonlinear process are not fully understood and need to be further investigated.
2. Detailed quantitative experimental studies of the instability on sharp cones are missing, with respect to both the primary instability and its breakdown.
3. Although the rotating cylinder can be seen as a limiting case of sharp cones, it is fundamentally different since there is no flow along the cylinder. However, Taylor–Couette–Poiseuille flow with the inner cylinder rotating and an axial flow through the annulus has clear similarities to, and could be used as a model for, flow on rotating sharp cones.
4. The most unstable mode on broad and sharp cones changes from cross flow to centrifugal flow around $\psi = 45^\circ$. The details of that changeover have so far not been studied and could provide interesting information about the behavior between competing instabilities.
5. Transition delay on swept wings caused by reducing the growth of cross-flow vortices is an important research topic. Deterministic triggering of wavenumbers amplified less than the most unstable one has been suggested as one way to achieve this delay (see also

Pier 2007). However, so far this has not been investigated on the rotating disk, which could serve as a less complicated experimental facility for such and other control studies, where surface modifications are explored.

6. Detailed experiments or simulations of turbulent boundary layers on the disk (and also on cones) at high Reynolds numbers would give important information on 3D turbulent boundary layer flows.
7. The present review deals with the flow around rotating bodies in an infinite still fluid; however, there are adjacent interesting flows that have not been discussed and are also less studied, such as a coflowing surrounding fluid, with or without angle of attack, and the flow around a rotating body in a stationary enclosure.

DISCLOSURE STATEMENT

The authors are not aware of any biases that might be perceived as affecting the objectivity of this review.

ACKNOWLEDGMENTS

We would like to acknowledge several coworkers who, during the last ten or more years, have worked with us on rotating disks and cones: Drs Shintaro Imayama, Ellinor Appelquist, Takuya Kawata, and Antonio Segalini, as well as Prof. Philipp Schlatter, all of whom are recognized in some of the review's cited papers. Our research within this area has mainly been supported by the Swedish Research Council (ASTRID and SERAFINA projects), but also from the Linné FLOW Centre, Carl Trygger Stiftelse, and JSPS (Japan Society for the Promotion of Science), among others.

LITERATURE CITED

- Al-Malki MAS, Fildes MR, Hussain Z. 2022. Competing roughness effects on the nonstationary crossflow instability of the boundary-layer over a rotating broad cone. *Phys. Fluids* 34:104103
- Appelquist E, Alfredsson PH, Schlatter P, Lingwood RJ. 2016a. On the global nonlinear instability of the rotating-disk flow over a finite domain. *J. Fluid Mech.* 803:332–55
- Appelquist E, Imayama S, Alfredsson PH, Schlatter P, Lingwood RJ. 2016b. Linear disturbances in the rotating-disk flow: a comparison between results from simulations, experiments and theory. *Eur. J. Mech. B* 55:170–81
- Appelquist E, Schlatter P, Alfredsson PH, Lingwood RJ. 2015. Global linear instability of the rotating-disk flow investigated through simulations. *J. Fluid Mech.* 765:612–31
- Appelquist E, Schlatter P, Alfredsson PH, Lingwood RJ. 2018a. Turbulence in the rotating-disk boundary layer investigated through direct numerical simulations. *Eur. J. Mech. B* 70:6–18
- Appelquist E, Schlatter P, Alfredsson PH, Lingwood RJ. 2018b. Transition to turbulence in the rotating-disk boundary-layer flow with stationary vortices. *J. Fluid Mech.* 836:43–71
- Benton ER. 1966. On the flow due to a rotating disk. *J. Fluid Mech.* 24:781–800
- Bödewadt UT. 1940. Die Drehströmung über festem Grund. *Z. Angew. Math. Mech.* 20:241–53
- Carpenter PW, Thomas PJ. 2007. Flow over compliant rotating disks. *J. Eng. Math.* 57:303–15
- Cham TS, Head MR. 1969. Turbulent boundary-layer flow on a rotating disk. *J. Fluid Mech.* 37:129–47
- Chiang C, Eaton JK. 1996. An experimental study of the effects of three-dimensionality on the near wall turbulence structures using flow visualization. *Exp. Fluids* 20:266–72
- Chicchiero C, Segalini A, Camarri S. 2021. Triple-deck analysis of the steady flow over a rotating disk with surface roughness. *Phys. Rev. Fluids* 6:014103

- Cooper AJ, Harris JH, Garrett SJ, Özkan M, Thomas PJ. 2015. The effect of anisotropic and isotropic roughness on the convective stability of the rotating disk boundary layer. *Phys. Fluids* 27:014107
- Corke TC, Knasiak KF. 1998. Stationary travelling cross-flow mode interactions on a rotating disk. *J. Fluid Mech.* 355:285–315
- Crespo del Arco E, Serre E, Bontoux P, Launder BE. 2005. Stability, transition and turbulence in rotating cavities. In *Instability of Flows*, ed. M Rahman, pp. 141–95. Adv. Fluid Mech. 41. Southampton, UK: WIT Press
- Ekman VW. 1905. On the influence of the earth's rotation on ocean currents. *Ark. Mat. Astron. Fys.* 2:1–52
- Erian FF, Tong YH. 1971. Turbulent flow due to a rotating disk. *Phys. Fluids* 14:2588–91
- Garrett SJ, Cooper AJ, Harris JH, Özkan M, Segalini A, Thomas PJ. 2016. On the stability of von Kármán rotating-disk boundary layers with radial anisotropic surface roughness. *Phys. Fluids* 28:014104
- Garrett SJ, Hussain Z, Stephen SO. 2009. The cross-flow instability of the boundary layer on a rotating cone. *J. Fluid Mech.* 622:209–32
- Garrett SJ, Peake N. 2007. The absolute instability of the boundary layer on a rotating cone. *Eur. J. Mech. B* 26:344–53
- Gregory N, Stuart JT, Walker WS. 1955. On the stability of three-dimensional boundary layers with application to the flow due to a rotating disk. *Philos. Trans. R. Soc. A* 248:155–99
- Harris J, Thomas P, Garrett S. 2012. *On the stability of flows over rough rotating disks*. Paper presented at AIAA Fluid Dynamics Conference and Exhibit, 42nd, New Orleans, La., AIAA Pap. 2012-3075
- Healey JJ. 2010. Model for unstable global modes in the rotating-disk boundary layer. *J. Fluid Mech.* 663:148–59
- Huerre P, Monkewitz PA. 1990. Local and global instabilities in spatially developing flows. *Annu. Rev. Fluid Mech.* 22:473–537
- Hussain Z, Garrett SJ, Stephen SO. 2014. The centrifugal instability of the boundary-layer flow over slender rotating cones. *J. Fluid Mech.* 755:274–93
- Imayama S, Alfredsson PH, Lingwood RJ. 2012. A new way to describe the transition characteristics of a rotating-disk boundary-layer flow. *Phys. Fluids* 24:031701
- Imayama S, Alfredsson PH, Lingwood RJ. 2013. An experimental study of edge effects on rotating-disk transition. *J. Fluid Mech.* 716:638–57
- Imayama S, Alfredsson PH, Lingwood RJ. 2014a. On the laminar–turbulent transition of the rotating-disk flow: the role of absolute instability. *J. Fluid Mech.* 745:132–63
- Imayama S, Lingwood RJ, Alfredsson PH. 2014b. The turbulent rotating-disk boundary layer. *Eur. J. Mech. B* 48:245–53
- Imayama S, Alfredsson PH, Lingwood RJ. 2016. Experimental study of rotating-disk boundary-layer flow with surface roughness. *J. Fluid Mech.* 786:5–28
- Itoh M, Hasegawa I. 1994. Turbulent boundary layer on a rotating disk in infinite quiescent fluid. *JSMI Int. J. B* 37:449–56
- Jarre S, Le Gal P, Chauve MP. 1996. Experimental study of rotating disk flow instability. II. Forced flow. *Phys. Fluids* 8:2985–94
- Kato K, Alfredsson PH, Lingwood RJ. 2019a. Boundary-layer transition over a rotating broad cone. *Phys. Rev. Fluids* 4:071902
- Kato K, Alfredsson PH, Lingwood RJ. 2023. Rotating disks and cones—a centennial of von Kármán's 1921 paper. *J. Fluid Sci. Technol.* 18(1):JFST0003
- Kato K, Kawata T, Alfredsson PH, Lingwood RJ. 2019b. Investigation of the structures in the unstable rotating-cone boundary layer. *Phys. Rev. Fluids* 4:053903
- Kato K, Segalini A, Alfredsson PH, Lingwood RJ. 2021. Instability and transition in the boundary layer driven by a rotating slender cone. *J. Fluid Mech.* 915:R4
- Kato K, Segalini A, Alfredsson PH, Lingwood RJ. 2022. Instabilities and transition on a rotating cone—old problems and new challenges. In *IUTAM Laminar-Turbulent Transition: 9th IUTAM Symposium, London, UK, Sept. 2–6, 2019*, ed. S Sherwin, P Schmid, X Wu, pp. 203–13. Cham, Switz.: Springer
- Kirchner RP, Chen CF. 1970. Stability of time-dependent rotational Couette flow. Part 1. Experimental investigation. *J. Fluid Mech.* 40:39–47

- Kobayashi R. 1994. Review: laminar-to-turbulent transition of three-dimensional boundary layers on rotating bodies. *J. Fluid. Eng.* 116:200–11
- Kobayashi R, Izumi H. 1983. Boundary-layer transition on a rotating cone in still fluid. *J. Fluid Mech.* 127:353–64
- Kobayashi R, Kohama Y, Takamadate C. 1980. Spiral vortices in boundary layer transition regime on a rotating disk. *Acta Mech.* 35:71–82
- Kohama YP. 2000. Three-dimensional boundary layer transition study. *Curr. Sci. India* 79:800–7
- Lee K, Nishio Y, Izawa S, Fukunishi Y. 2018. The effect of downstream turbulent region on the spiral vortex structures of a rotating-disk flow. *J. Fluid Mech.* 266:175–207
- Lingwood RJ. 1995. Absolute instability of the boundary layer on a rotating disk. *J. Fluid Mech.* 299:17–33
- Lingwood RJ. 1996. An experimental study of absolute instability of the rotating-disk boundary-layer flow. *J. Fluid Mech.* 314:373–405
- Lingwood RJ. 1997. Absolute instability of the Ekman layer and related rotating flows. *J. Fluid Mech.* 331:405–28
- Lingwood RJ, Alfredsson PH. 2000. Experimental study of the stability of the Bödewadt layer. In *Laminar-Turbulent Transition: IUTAM Symposium, Sedona/AZ Sept. 13–17, 1999*, ed. HF Fasel, WS Saric, pp. 553–58. Berlin: Springer
- Lingwood RJ, Alfredsson PH. 2015. Instabilities of the von Kármán boundary layer. *Appl. Mech. Rev.* 67:030803
- Littell HS, Eaton JK. 1994. Turbulence characteristics of the boundary layer on a rotating disk. *J. Fluid Mech.* 266:175–207
- Malik MR, Wilkinson SP, Orszag SA. 1981. Instability and transition in rotating disk flow. *ALAA J.* 19:1131–38
- Martinand D, Serre E, Viaud B. 2023. Instabilities and routes to turbulence in rotating disc boundary layers and cavities. *Philos. Trans. R. Soc. A* 381:20220135
- Miklavčič M, Wang CY. 2004. The flow due to a rough rotating disk. *Z. Angew. Math. Phys.* 54:235–46
- Pier B. 2003. Finite-amplitude crossflow vortices, secondary instability and transition in the rotating-disk boundary layer. *J. Fluid Mech.* 487:315–43
- Pier B. 2007. Primary crossflow vortices, secondary absolute instabilities and their control in the rotating-disk boundary layer. *J. Eng. Math.* 57:237–51
- Randriamampianina A, Poncet S. 2006. Turbulence characteristics of the Bödewadt layer in a large enclosed rotor-stator system. *Phys. Fluids* 18:055104
- Saric WS, Reed HL, White EB. 2003. Stability and transition of three-dimensional boundary layers. *Annu. Rev. Fluid Mech.* 35:413–40
- Savaş O. 1987. Stability of the Bödewadt flow. *J. Fluid Mech.* 183:77–94
- Schlatter P, Örlü R. 2010. Assessment of direct numerical simulation data of turbulent boundary layers. *J. Fluid Mech.* 659:116–26
- Segalini A, Camarri S. 2019. Flow induced by a rotating cone: base flow and convective stability analysis. *Phys. Rev. Fluids* 4:084801
- Siegmund-Schultze R. 2020. “The joy that engineers and mathematicians have come together.” Richard von Mises’ foundation of ZAMM, and its “Tasks and Goals” (1920/21). *Z. Angew. Math. Mech.* 100(2):e202002017
- Smith NH. 1947. *Exploratory investigation of laminar-boundary-layer oscillations on a rotating disk*. NACA Tech. Note 1227, Natl. Adv. Commit. Aeronaut., Langley Aeronaut. Lab., Langley Field, VA
- Theodorsen T, Regier A. 1944. *Experiments on drag of revolving disks, cylinders, and streamline rods at high speeds*. NACA Tech. Rep. 793, Natl. Adv. Commit. Aeronaut., Langley Aeronaut. Lab., Langley Field, VA
- von Kármán T. 1921. Über laminare und turbulente Reibung. *Z. Angew. Math. Mech.* 1:233–52
- von Kármán T. 1946. *On laminar and turbulent friction*. NACA Tech. Mem. 1092, Natl. Adv. Commit. Aeronaut., Washington, DC
- Watanabe T. 1989. Effect of surface roughness on boundary layer transition in a rotating disk. *Trans. Jpn. Soc. Mech. Eng. B* 55:1842–46 (In Japanese)

- Watanabe T, Warui HM, Fujisawa N. 1993. Effect of distributed roughness on laminar-turbulent transition in the boundary layer over a rotating cone. *Exp. Fluids* 14:390–92
- Wimmer M. 1988. Viscous flows and instabilities near rotating bodies. *Prog. Aerosp. Sci.* 25:43–103
- Wu CS. 1959. The three dimensional incompressible laminar boundary layer on a spinning cone. *Appl. Sci. Res. A* 8:140–46
- Yoon M, Hyun J, Park J. 2007. Flow and heat transfer over a rotating disk with surface roughness. *Int. J. Heat Fluid Flow* 28:262–67